



HAL
open science

Understanding the Nature of the Optical Emission in Gamma-Ray Bursts: Analysis from TAROT, COATLI, and RATIR Observations

R.L Becerra, A Klotz, J.L Atteia, D Guetta, A.M Watson, F de Colle, C Angulo-Valdez, N.R Butler, S Dichiara, N Fraija, et al.

► **To cite this version:**

R.L Becerra, A Klotz, J.L Atteia, D Guetta, A.M Watson, et al.. Understanding the Nature of the Optical Emission in Gamma-Ray Bursts: Analysis from TAROT, COATLI, and RATIR Observations. *Monthly Notices of the Royal Astronomical Society*, 2023, 525 (3), pp.3262-3273. 10.1093/mnras/stad2513 . hal-04191093

HAL Id: hal-04191093
















<https://hal.science/hal-04191093>

Submitted on 5 Jan 2024

HAL is a multi-disciplinary open access archive for the deposit and dissemination of scientific research documents, whether they are published or not. The documents may come from teaching and research institutions in France or abroad, or from public or private research centers.

L'archive ouverte pluridisciplinaire **HAL**, est destinée au dépôt et à la diffusion de documents scientifiques de niveau recherche, publiés ou non, émanant des établissements d'enseignement et de recherche français ou étrangers, des laboratoires publics ou privés.

Understanding the nature of the optical emission in gamma-ray bursts: analysis from TAROT, COATLI, and RATIR observations

R. L. Becerra ¹★, A. Klotz ², J. L. Atteia ²★, D. Guetta ³, A. M. Watson ⁴★, F. De Colle ¹,
C. Angulo-Valdez ⁴, N. R. Butler ⁵, S. Dichiara ⁶, N. Fraija ⁴, K. Garcia-Cifuentes ¹,
A. S. Kutyrév ^{7,8}, W. H. Lee ⁴, M. Pereyra ⁹ and E. Troja ¹⁰

¹Instituto de Ciencias Nucleares, Universidad Nacional Autónoma de México, Apartado Postal 70-264, 04510 México, CDMX, Mexico

²IRAP, Université de Toulouse, CNRS, CNES, UPS, 31401, Toulouse, France

³Department of Physics, Ariel University, Ariel, 40700, Israel

⁴Instituto de Astronomía, Universidad Nacional Autónoma de México, Apartado Postal 70-264, 04510 México, CDMX, Mexico

⁵School of Earth and Space Exploration, Arizona State University, Tempe, AZ 85287, USA

⁶Department of Astronomy and Astrophysics, The Pennsylvania State University, 525 Davey Lab, University Park, PA 16802, USA

⁷Department of Astronomy, University of Maryland, College Park, MD 20742-4111, USA

⁸Astrophysics Science Division, NASA Goddard Space Flight Center, 8800 Greenbelt Road, Greenbelt, MD 20771, USA

⁹CONACYT, Instituto de Astronomía, Universidad Nacional Autónoma de México, 22860 Ensenada, BC, Mexico

¹⁰Department of Physics, University of Rome – Tor Vergata, via della Ricerca Scientifica 1, I-00100 Rome, Italy

Accepted 2023 August 16. Received 2023 August 11; in original form 2023 June 30

ABSTRACT

We collected the optical light-curve data of 227 gamma-ray bursts (GRBs) observed with the TAROT, COATLI, and RATIR telescopes. These consist of 133 detections and 94 upper limits. We constructed average light curves in the observer and rest frames in both X-rays (from *Swift*/X-Ray Telescope) and the optical. Our analysis focused on investigating the observational and intrinsic properties of GRBs. Specifically, we examined observational properties, such as the optical brightness function of the GRBs at $T = 1000$ s after the trigger, as well as the temporal slope of the afterglow. We also estimated the redshift distribution for the GRBs within our sample. Of the 227 GRBs analysed, we found that 116 had a measured redshift. Based on these data, we calculated a local rate of $\rho_0 = 0.2 \text{ Gpc}^{-3} \text{ yr}^{-1}$ for these events with $z < 1$. To explore the intrinsic properties of GRBs, we examined the average X-ray and optical light curves in the rest frame. We use the AFTERGLOWPY LIBRARY to generate synthetic curves to constrain the parameters typical of the bright GRB jet, such as energy ($\langle E_0 \rangle \sim 10^{53.6}$ erg), opening angle ($\langle \theta_{\text{core}} \rangle \sim 0.2$ rad), and density ($\langle n_0 \rangle \sim 10^{-2.1} \text{ cm}^{-3}$). Furthermore, we analyse microphysical parameters, including the fraction of thermal energy in accelerated electrons ($\langle \epsilon_e \rangle \sim 10^{-1.37}$) and in the magnetic field ($\langle \epsilon_B \rangle \sim 10^{-2.26}$), and the power-law index of the population of non-thermal electrons ($\langle p \rangle \sim 2.2$).

Key words: (stars:) gamma-ray burst: individual: GRB 180706A – (stars:) gamma-ray burst: individual: GRB 180812A – (stars:) gamma-ray bursts: general.

1 INTRODUCTION

Gamma-ray bursts (GRBs) are the brightest electromagnetic events observed in the Universe (Atteia et al. 2017; O’Connor et al. 2023). These bursts can be classified into two distinct populations: long GRBs (LGRBs) and short GRBs (SGRBs; Kouveliotou et al. 1993). This classification is based primarily on the duration T_{90} , which represents the time interval that encompasses 90 per cent of the total observed counts in gamma-rays. LGRBs (with $T_{90} \gtrsim 2$ s) are associated with the collapse of massive stars (e.g. Woosley 1993; MacFadyen & Woosley 1999), whereas SGRBs (with $T_{90} \lesssim 2$ s) are believed to result from the coalescence of two compact objects (e.g. Paczynski 1986, 1991; Lee & Ramirez-Ruiz 2007; Abbott et al. 2017).

The fireball model (Sari, Piran & Narayan 1998) is the standard theory used to explain most of the features observed in the GRB

light curves. This model describes both the prompt emission and the afterglow phase. During the prompt phase, the rapid variability is produced by internal shocks in the jet (Rees & Meszaros 1994; Kobayashi, Piran & Sari 1997), by photospheric emission (Thompson 1994; Eichler & Levinson 2000), or by magnetic reconnection (Metzger et al. 2011; Zhang & Yan 2011). As the jet interacts with the circumburst medium, it decelerates, generating the afterglow phase. This phase is characterized by synchrotron emission, where relativistic electrons are continuously accelerated by an ongoing shock that interacts with the surrounding medium (Granot et al. 2002). This blast wave creates a forward shock that propagates through the surrounding medium and a reverse shock that propagates through the shell (Sari et al. 1998).

The emission of the afterglow can be described by power-law segments of the flux $F \propto t^{-\alpha} \nu^{-\beta}$, where t , ν , α , and β represent time, frequency, temporal index, and spectral index, respectively (Sari et al. 1998; Granot et al. 2002).

* E-mail: rosa.becerra@correo.nucleares.unam.mx (RLB);
jean-luc.atteia@irap.omp.eu (JLA); alan@astro.unam.mx (AMW)

With the launch of the *Swift* mission in 2004, our understanding of afterglows has greatly expanded (Gehrels et al. 2004). This is largely due to the monitoring provided by the X-Ray Telescope (XRT), which has provided an abundance of data from the very beginning of the afterglow. Unlike lower frequencies, the large amount of X-ray data has enabled both statistical studies and in-depth investigations of the light curves of GRBs at these energies (Burrows et al. 2005).

The observational phases of X-ray afterglows can generally be identified as follows: a steep decay phase related to the end of the prompt emission phase; a shallow decay phase (or plateau) commonly interpreted as a signature of late-time energy injection; a normal decay phase; and a jet-break steepening given by a geometric effect related to the observer seeing the edge of the jet at late times. Additionally, flares are sometimes observed (see e.g. Nousek et al. 2006; Zhang et al. 2006; Evans et al. 2009). These flares are believed to be produced by the central engine in a manner analogous to the prompt emission (Burrows et al. 2005).

However, observing the GRB early optical emission by ground telescopes is not an easy task. This is because GRBs (in their prompt emission phase) are short-lived, lasting only a few seconds to a few minutes, and most ground-based telescopes simply cannot respond quickly enough to capture their first seconds. Moreover, the telemetry delays in receiving alerts from the General Coordinates Network/Transient Astronomy Network (GCN/TAN)¹ result in the loss of early information from GRBs at these frequencies.

Therefore, the sample size of the early optical phases of the GRB remains considerably smaller compared to the later afterglows (see e.g. Kann et al. 2010; Li et al. 2012; Wang et al. 2013). Despite this limitation, these samples provide valuable insight into the diverse range of apparent brightness values observed during the early phases of GRBs. In some cases, extremely faint nearby GRBs have been observed (see e.g. Liang et al. 2007), while in other cases, the observed brightness is much higher than expected (see e.g. Perley et al. 2014; Becerra et al. 2023; O'Connor et al. 2023), reaching apparent magnitudes of approximately $r = 14$ – 16 (see e.g. Klotz et al. 2009; Pereyra et al. 2022). This suggests that the observed brightness is not solely dependent on the distance.

Moreover, not all GRBs have an optical counterpart, and the reason for this darkness has been widely discussed (see e.g. Greiner et al. 2011). Possible explanations have been proposed by Lang et al. (2010): (i) the intrinsically low luminosity of the GRB; (ii) the environment surrounding the GRB; and (iii) the high absorption of intergalactic medium due to large distances ($z > 6$).

Small aperture, fast slewing telescopes are usually used for observations of optical counterparts of GRBs (see e.g. Klotz et al. 2006; Becerra et al. 2019a), whereas larger aperture telescopes are necessary for detecting the afterglow when it has faded. In this paper, following this pattern, we use early optical data from the COATLI and Télescopes à Action Rapide pour les Objets Transitoires (TAROT) telescopes and late data from the Reionization and Transients Infrared/Optical Project (RATIR; see e.g. Becerra et al. 2019b). We aim to describe the observational properties of a sample of early optical afterglows followed by COATLI, TAROT, and RATIR. We describe each of them in Section 2 and the complete sample in Section 3. We present the phenomenological results in Section 4: the brightness function at $T + 1000$ s and the subsequent analysis at the early phases of the afterglow. In this section, we also compare the X-ray and optical flux to classify the events of our sample as dark or not. Additionally, we analyse the redshift distribution of our sample in Section 5. Finally, we discuss and summarize our conclusions in Section 6.

2 TELESCOPES

2.1 TAROT

TAROT² is an automated telescope network located at different sites around the world with automated observations (without human interaction). TAROT was first designed as a robotic observatory in 1995. The Calern (TCA) observatory in France hosted the first TAROT, and its first light was in 1998. TAROT subsequently expanded to two other sites: La Silla, Chile (TCH) and La Reunión (TRE). TCA and TCH have a field of view (FoV) of $1.8 \text{ deg}^2 \times 1.8 \text{ deg}^2$, whereas the FoV of TRE is $4.2 \text{ deg}^2 \times 4.2 \text{ deg}^2$. TCA and TCH have a limiting R magnitude of $R = 18.2$ at 5σ for unfiltered exposures of 1 min, whereas the limiting R magnitude of TRE is $R = 17$. The goal of this consortium is the very early observations of GRB optical counterparts (Klotz et al. 2006). TAROT is connected to the GCN/TAN alert system and its first exposure is trailed with a duration of 60 s to allow continuous monitoring of the light curve. For these exposures, the tracking of the hour-angle motor was adapted to give a drift of $0.30 \text{ pixels s}^{-1}$. As a consequence, stars trail with a length of about 18 pixels on the image and the flux is recorded continuously without dead time (Klotz et al. 2006). Subsequent exposures are typically conventional and do have a small amount of dead time.

2.2 COATLI

COATLI³ is an ASTELCO 50-cm Richey-Crétien telescope on a fast ASTELCO NTM-500 German equatorial mount at the Observatorio Astronómico Nacional on Sierra de San Pedro Mártir in Baja California, Mexico (Cuevas et al. 2016; Watson et al. 2016).

COATLI is connected to the GCN/TAN alert system and observes GRBs autonomously. The reduction pipeline (Becerra et al. 2019a) performs bias subtraction, dark subtraction, flat-field correction, and cosmic ray cleaning with the *cosmicrays* task in IRAF (Tody 1986). We perform astrometric calibration of our images using the *astrometry.net* software (Lang et al. 2010). We calibrate against the U.S. Naval Observatory B-1.0 Catalog (USNO-B1) (Monet et al. 2003) and the Panoramic Survey Telescope and Rapid Response System (Pan-STARRS) DR1 (Magnier et al. 2020).

The COATLI w photometry is well described by $(w - r') = 0.353(g' - r') - 0.243(g' - r')^2$, where the prime symbols in g' and r' refer to Sloan Digital Sky Survey (SDSS) magnitudes (Becerra et al. 2019a).

2.3 RATIR

RATIR⁴ was a four-channel simultaneous optical and near-infrared imager mounted on the 1.5-m Harold L. Johnson Telescope at the Observatorio Astronómico Nacional in Sierra San Pedro Mártir in Baja California, Mexico. It was operated from 2012 April to 2022 June. RATIR responded autonomously to GRB triggers from the Burst Alert Telescope (*Swift*/BAT) instrument and obtained simultaneous photometry in *riZJ* or *riYH* (Butler et al. 2012; Watson et al. 2012; Littlejohns et al. 2015; Becerra et al. 2017).

The reduction pipeline (Littlejohns et al. 2015) performs bias subtraction and flat-field correction, followed by astrometric calibration using the *astrometry.net* software (Lang et al. 2010), iterative sky subtraction, co-addition using SWARP (Bertin 2010), and source detection using SEXTRACTOR (Bertin & Arnouts 1996). We calibrate

²<http://tarot.obs-hp.fr/>

³<http://coatli.astrosco.unam.mx/>

⁴<http://ratir.astrosco.unam.mx/>

¹<https://gcn.gsfc.nasa.gov/about.html>

Table 1. COATLI observations of GRB 180706A.

T (s)	Exposure (s)	w (AB)
615	5	17.07 ± 0.14
624	5	17.17 ± 0.13
634	5	17.11 ± 0.13

Table 2. COATLI observations of GRB 180812A.

T (s)	Exposure (s)	w (AB)
46	5	16.82 ± 0.14
55	5	16.79 ± 0.13
65	5	16.70 ± 0.12
74	5	16.83 ± 0.14
83	5	16.85 ± 0.14
92	5	16.74 ± 0.13
101	5	16.52 ± 0.11
110	5	16.61 ± 0.12
119	5	16.76 ± 0.13
128	5	16.61 ± 0.11
141	5	16.76 ± 0.13
150	5	16.59 ± 0.11
159	5	16.73 ± 0.12
168	5	16.59 ± 0.11
177	5	16.72 ± 0.12
186	5	16.79 ± 0.13
195	5	16.73 ± 0.12
204	5	16.75 ± 0.12
215	5	16.58 ± 0.11
224	5	17.03 ± 0.16
237	5	16.76 ± 0.13
246	5	17.01 ± 0.16
255	5	17.19 ± 0.19
264	5	16.95 ± 0.15
273	5	17.05 ± 0.16
282	5	17.21 ± 0.19
291	5	17.22 ± 0.19
300	5	17.74 ± 0.31
309	5	17.16 ± 0.18
318	5	17.25 ± 0.20
331	5	17.07 ± 0.17
340	5	17.30 ± 0.21
349	5	17.23 ± 0.19
358	5	17.36 ± 0.22
367	5	17.53 ± 0.25
376	5	17.32 ± 0.21
385	5	17.40 ± 0.23
394	5	17.45 ± 0.23
403	5	17.19 ± 0.19
412	5	17.33 ± 0.21
426	5	17.25 ± 0.20

against SDSS DR9 (Ahn et al. 2012) and Two Micron All-Sky Survey (2MASS) (Skrutskie et al. 2006).

3 DATA SAMPLE

We used all available optical photometric data from TAROT, RATIR, and COATLI. TAROT and COATLI use clear filters, whereas the RATIR uses *griZYJH* photometry system. For typical GRBs, the AB magnitudes in the TAROT and COATLI clear filters (w filters) are approximately the same as those in the RATIR r filter (see e.g. Becerra et al. 2019b, c, 2021). We present new COATLI photometry of GRB 180706A (see Table 1) and GRB 180812A (see Table 2).

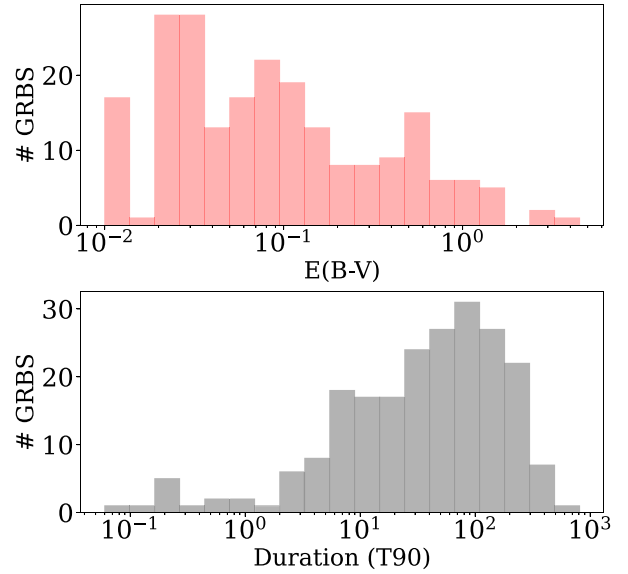


Figure 1. Histograms of reddening values $E(B - V)$ (top panel) and duration T_{90} (bottom panel).

The complete information for each event is described in Table 3. The first column shows the name of the GRB, the second the *Swift*/BAT trigger, and the third, fourth, and fifth columns list the redshift z , the extinction value $E(B - V)$, and the duration T_{90} , respectively. The information on the redshift z , reddening $E(B - V)$, and duration T_{90} was retrieved from the GCN/TAN circulars and the *Swift*/BAT repository.⁵ To calculate the extinction A_r , we use the relationship $A_V = 3.1 \times E(B - V)$ and (Schlegel, Finkbeiner & Davis 1998) and $A_r/A_V \approx 0.9$ (Gordon et al. 2003). We illustrate the histograms of duration and reddening in Fig. 1.

For the sample used in this study, we have 13 SGRBs and 205 LGRBs according to the parameter T_{90} . Furthermore, the *Swift* catalogue⁶ Lien 2016 gives redshifts for 116 out of 227 events, that is, 51 per cent of the sample. To find out if this sample is representative of the total population of GRBs, we compared the cumulative distribution of the redshifts of GRBs detected in our sample (see Table 3) and the redshift values in the catalogue of all GRBs detected by the *Swift*/BAT instrument. We plot this comparison in Fig. 2. The similarity between the two curves was quantified by a Kolmogorov–Smirnov test, which gave a p -value of 0.69. Therefore, we conclude that both distributions are similar and that the results obtained in this work with the population studied here is not biased in redshift compared with whole *Swift* sample. This distribution is analysed in detail in Section 5.1.

4 PHENOMENOLOGICAL RESULTS

A total of 227 events were collected from the COATLI, RATIR, and TAROT data bases, of which 133 were detections, and the remaining 94 were only upper limits, all of which are shown in Fig. 3. The first image was captured, on average, about 150 s after the trigger, with an initial AB magnitude of around $r = 16.5$. In Fig. 3, we also show the average optical light curve of prompt emission and early

⁵https://swift.gsfc.nasa.gov/results/batgrbcats/index_tables.html

⁶https://swift.gsfc.nasa.gov/results/batgrbcats/summary_cflux/summary_general_info/GRBlist_redshift_BAT.txt

Table 3. Properties of GRBs used in this work.

GRB	Trigger	$E(B - V)$	z	T_{90} (s)
GRB 050525A	130088	–	–	8.83 ± 0.07
GRB 060124	178750	0.13	–	13.42 ± 1.29
GRB 060209	180931	0.93	–	–
GRB 060512	209755	0.02	2.10	8.40 ± 1.73
GRB 060515	210084	0.03	–	52.37 ± 5.48
GRB 060814	224552	0.04	1.92	145.07 ± 4.82
GRB 060825	226382	0.57	–	7.98 ± 0.66
GRB 060904A	227996	0.02	2.55	80.06 ± 2.22
GRB 060904B	228006	0.17	0.70	189.98 ± 21.16
GRB 060919	230115	0.07	–	9.00 ± 1.67
GRB 061019	234516	1.14	–	180.38 ± 6.36
GRB 061027	235645	0.03	–	105.81 ± 36.94
GRB 061028	235715	0.16	–	105.81 ± 36.94
GRB 061109	237821	0.19	–	–
GRB 061110B	238174	0.09	3.43	135.25 ± 17.59
GRB 061217	251634	0.04	0.83	0.22 ± 0.04
GRB 061218	251863	0.12	–	–
GRB 061222B	252593	0.41	3.35	37.25 ± 6.06
GRB 070103	254532	0.07	2.62	18.41 ± 1.21
GRB 070227	262347	0.22	–	3.20 ± 1.60
GRB 070330	273180	0.06	–	6.64 ± 0.67
GRB 070411	275087	0.10	2.95	115.69 ± 16.87
GRB 070412	275119	0.02	–	33.88 ± 5.08
GRB 070420	276321	0.52	3.01	77.02 ± 5.47
GRB 070508	278854	0.03	0.82	20.9 ± 0.73
GRB 070521	279935	0.03	2.09	38.63 ± 2.38
GRB 070610	281993	0.81	–	–
GRB 070621	282808	0.05	–	33.26 ± 2.51
GRB 070628	283320	0.77	–	39.08 ± 4.07
GRB 070913	290843	0.13	–	2.68 ± 0.56
GRB 070920A	291614	0.10	–	55.76 ± 5.29
GRB 070920B	291728	0.01	–	22.26 ± 2.79
GRB 071010A	293707	0.42	0.98	6.32 ± 1.87
GRB 071101	295779	1.29	–	4.82 ± 1.97
GRB 071112C	296504	1.29	0.82	44.8 ± 1.60
GRB 080129	301981	1.02	4.35	50.18 ± 9.17
GRB 080207	302728	0.02	2.08	292.46 ± 7.99
GRB 080210	302888	0.08	2.64	42.26 ± 11.37
GRB 080315	306323	0.13	–	–
GRB 080330	308041	0.02	1.51	60.36 ± 36.4
GRB 080413A	309096	0.16	2.43	46.36 ± 0.48
GRB 080430	310613	0.01	0.77	13.87 ± 1.90
GRB 080516	311762	0.35	3.20	5.76 ± 0.22
GRB 080603B	313087	0.01	2.69	59.12 ± 1.63
GRB 080727C	318170	0.07	–	77.36 ± 7.04
GRB 080903	323542	0.22	–	66.34 ± 10.42
GRB 081003B	325080	0.64	–	30.00
GRB 081028A	332851	0.03	3.04	284.42 ± 30.55
GRB 081109A	334112	0.02	0.98	221.49 ± 58.97
GRB 081126	335647	0.68	–	57.65 ± 5.85
GRB 081228	338338	0.16	3.44	3.00 ± 1.41
GRB 090102	338895	0.03	1.55	28.32 ± 2.35
GRB 090307A	345551	0.53	–	22.00 ± 6.40
GRB 090313	346386	0.03	3.37	83.04 ± 19.48
GRB 090519	352648	0.04	3.85	58.04 ± 8.18
GRB 091127	377179	0.04	0.49	6.96 ± 0.15
GRB 100316A	416076	0.03	3.15	6.75 ± 0.95
GRB 100816A	431764	0.09	0.80	2.88 ± 0.63
GRB 100915A	434178	0.51	–	199.20 ± 26.19
GRB 100917A	434360	0.09	–	63.82 ± 21.56
GRB 110128A	443861	0.01	2.34	14.15 ± 2.49
GRB 110205A	444643	0.01	2.22	249.42 ± 15.03
GRB 110207A	444912	0.03	–	82.58 ± 10.83
GRB 110422A	451901	0.03	1.77	25.78 ± 0.60

Table 3 – continued

GRB	Trigger	$E(B - V)$	z	T_{90} (s)
GRB 110520A	453747	0.03	–	20.86 ± 5.37
GRB 111209A	509336	0.02	0.68	810.97 ± 52.11
GRB 111225A	510341	0.26	0.30	105.73 ± 26.18
GRB 111228A	510649	0.03	0.72	101.24 ± 5.45
GRB 120106A	511235	1.19	–	63.50 ± 4.62
GRB 120119A	512035	0.11	1.73	68.00 ± 7.07
GRB 120324A	518507	1.12	1.10	118.42 ± 10.01
GRB 120326A	518626	0.05	1.80	69.48 ± 8.18
GRB 120327A	518731	0.34	2.81	63.53 ± 7.03
GRB 120328A	518792	0.73	–	29.93 ± 6.67
GRB 120403B	519256	0.13	–	7.28 ± 1.92
GRB 120514A	522197	1.63	–	164.34 ± 5.84
GRB 120521A	522578	0.43	–	0.51 ± 0.14
GRB 120521B	522586	0.45	–	146.83 ± 27.94
GRB 120521C	522656	0.01	5.93	27.07 ± 4.34
GRB 120805A	530031	0.03	3.10	48.00 ± 22.63
GRB 120807A	530267	1.41	–	19.88 ± 5.76
GRB 120811C	530689	0.03	2.67	24.34 ± 3.06
GRB 120815A	531003	0.10	2.36	7.23 ± 2.52
GRB 120816A	531223	0.96	–	4.43 ± 0.98
GRB 120909A	533060	0.09	3.93	220.6 ± 304.97
GRB 120913B	533613	0.06	–	122.59 ± 4.46
GRB 120922A	534394	0.15	3.10	168.22 ± 29.24
GRB 120923A	534402	0.16	7.84	26.08 ± 6.82
GRB 121024A	536580	0.1	2.30	67.97 ± 31.72
GRB 121108A	537921	0.37	–	89.55 ± 47.54
GRB 121202A	540255	0.05	–	19.54 ± 1.49
GRB 130131B	547420	0.03	2.54	4.30 ± 0.26
GRB 130215A	548760	0.10	0.60	66.22 ± 10.66
GRB 130216A	548927	0.49	–	6.52 ± 1.09
GRB 130327A	552063	0.13	–	6.37 ± 1.41
GRB 130418A	553847	0.03	1.22	274.92 ± 39.32
GRB 130420A	553977	0.01	1.30	121.14 ± 11.75
GRB 130427A	554620	0.24	0.34	244.33 ± 4.73
GRB 130505A	555163	0.04	2.27	89.34 ± 111.15
GRB 130514A	555821	0.23	3.60	214.19 ± 17.32
GRB 130521A	556344	0.52	–	10.96 ± 2.50
GRB 130603B	557310	0.02	0.36	0.18 ± 0.02
GRB 130605A	557508	0.36	–	10.18 ± 3.20
GRB 130606A	557589	0.02	5.91	276.66 ± 19.63
GRB 130610A	557845	0.02	2.09	47.72 ± 10.74
GRB 130612A	557976	0.08	2.01	4.00 ± 1.41
GRB 130615A	558271	0.12	–	332.56 ± 28.55
GRB 130722A	563213	0.63	–	98.37 ± 12.86
GRB 130907A	569992	0.01	1.24	364.37 ± 5.45
GRB 130925A	571830	0.02	0.35	160.30 ± 3.39
GRB 130929A	572308	2.58	–	12.24 ± 4.06
GRB 131105A	576738	0.03	1.69	112.21 ± 4.10
GRB 131117A	577968	0.02	4.04	10.88 ± 2.81
GRB 140114A	583861	0.02	3.00	139.95 ± 15.88
GRB 140215A	586680	0.09	–	25.63 ± 5.64
GRB 140302A	589685	0.52	–	98.72 ± 11.40
GRB 140304A	590206	0.08	5.28	14.78 ± 1.40
GRB 140311A	591390	0.03	4.95	70.48 ± 7.59
GRB 140320A	592544	0.51	–	0.51 ± 0.23
GRB 140331A	594081	0.05	4.65	209.66 ± 32.75
GRB 140413A	595616	0.02	–	132.98 ± 14.37
GRB 140419A	596426	0.03	3.96	80.08 ± 3.78
GRB 140423A	596901	0.01	3.26	134.14 ± 23.10
GRB 140516A	599188	0.02	–	0.26 ± 0.14
GRB 140518A	599287	0.02	4.71	60.52 ± 2.48
GRB 140610A	601259	2.56	–	93.25 ± 3.35
GRB 140622A	602278	0.07	0.96	0.13 ± 0.04
GRB 140626A	602604	0.15	–	16.16 ± 1.23

Table 3 – continued

GRB	Trigger	$E(B - V)$	z	T_{90} (s)
GRB 140703A	603243	0.10	3.14	68.64 ± 66.46
GRB 140709A	603810	0.40	–	105.19 ± 7.39
GRB 140710A	603954	0.06	0.56	3.00 ± 2.24
GRB 141004A	614390	0.32	0.57	3.92 ± 1.11
GRB 141015A	615399	0.51	–	11.00 ± 4.12
GRB 141022A	616061	0.10	–	8.72 ± 1.56
GRB 141031A	617110	0.17	–	464.00 ± 472.27
GRB 141109A	618024	0.04	2.99	200.19 ± 48.15
GRB 141121A	619182	0.05	1.47	481.00 ± 38.06
GRB 141221A	622006	0.03	1.45	36.82 ± 4.10
GRB 141225A	622476	0.02	0.91	86.15 ± 45.22
GRB 150203A	629578	0.90	–	24.44 ± 2.77
GRB 150213B	631051	0.02	–	209.00 ± 74.24
GRB 150323A	635887	0.03	0.59	149.73 ± 9.12
GRB 150323C	636005	0.01	–	159.66 ± 44.62
GRB 150716A	649157	1.43	–	42.57 ± 5.59
GRB 150727A	650530	–	0.31	87.96 ± 10.99
GRB 150728A	650617	0.20	–	0.83 ± 0.23
GRB 150811A	651882	0.17	–	31.52 ± 7.32
GRB 150817A	652334	0.48	–	38.00 ± 2.13
GRB 151215A	667392	0.39	2.59	17.85 ± 1.01
GRB 160117B	670800	0.07	0.87	11.54 ± 2.61
GRB 160121A	671231	0.53	1.96	10.50 ± 2.40
GRB 160123A	671447	0.10	–	3.95 ± 0.62
GRB 160127A	671828	0.06	–	6.16 ± 0.94
GRB 160131A	672236	0.11	0.97	327.75 ± 71.03
GRB 160203A	672525	0.07	3.52	17.44 ± 2.29
GRB 160220A	674670	0.13	–	8.26 ± 1.17
GRB 160225A	675998	0.01	–	157.46 ± 70.49
GRB 160228A	676595	0.06	1.64	98.91 ± 23.89
GRB 160313A	678929	0.01	–	41.54 ± 6.18
GRB 160314A	679120	0.08	0.73	8.73 ± 1.52
GRB 160321A	680017	0.75	–	33.48 ± 4.83
GRB 160327A	680655	0.01	4.99	33.74 ± 9.37
GRB 160410A	682269	0.02	1.72	96.00 ± 50.6
GRB 160501A	684679	0.18	–	118.00 ± 19.00
GRB 160504A	685124	0.01	–	53.96 ± 5.68
GRB 160506A	685245	0.26	–	260.53 ± 78.32
GRB 160630A	702252	0.48	–	29.55 ± 5.61
GRB 160705B	703176	0.01	–	54.58 ± 12.57
GRB 160714A	704310	0.02	–	0.35 ± 0.11
GRB 160821A	709351	0.03	–	112.64 ± 1.10
GRB 161004A	715084	0.25	–	1.32 ± 0.30
GRB 161014A	717500	0.08	2.82	23.00 ± 4.47
GRB 161022A	718655	0.04	–	7.25 ± 1.07
GRB 161105A	720697	0.33	–	177.70 ± 25.07
GRB 161108A	721234	0.02	0.50	115.84 ± 11.66
GRB 161117A	722604	0.06	1.55	125.70 ± 1.09
GRB 161214B	726885	0.08	<1.5	24.90 ± 3.18
GRB 161217A	727167	0.01	–	12.04 ± 2.45
GRB 161218A	727288	–	–	7.20 ± 0.55
GRB 170112A	732188	0.02	<0.2 ^a	0.06 ± 0.02
GRB 170202A	736407	0.02	3.64	37.76 ± 11.72
GRB 170317A	742866	0.19	–	11.95 ± 4.87
GRB 170318B	743086	4.51	–	1.07 ± 0.22
GRB 170405A	745797	0.09	3.51	165.31 ± 32.89
GRB 170409A	748858	–	–	68
GRB 170428A	750298	0.06	0.45	0.20 ± 0.07
GRB 170519A	753445	0.03	0.82	220.25 ± 143.84
GRB 170604A	755867	0.04	1.33	26.53 ± 2.84
GRB 170705A	760064	0.02	2.01	223.20 ± 15.55
GRB 170823A	769177	–	–	69.41 ± 12.03
GRB 170921A	773509	0.05	–	28.80 ± 5.93
GRB 171011A	778154	–	–	2.28 ± 0.23

Table 3 – continued

GRB	Trigger	$E(B - V)$	z	T_{90} (s)
GRB 171013A	778435	0.64	–	18.90 ± 1.50
GRB 171020A	780845	0.19	1.87	41.86 ± 9.19
GRB 171205A	794972	0.05	0.04	190.47 ± 33.88
GRB 180111A	804692	0.01	–	50.89 ± 1.88
GRB 180205A	808625	0.03	1.41	15.54 ± 3.15
GRB 180224A	811561	0.01	–	10.92 ± 3.57
GRB 180314A	814129	0.08	1.44	50.46 ± 21.84
GRB 180316A	814677	0.28	–	87.00 ± 20.59
GRB 180325A	817564	0.02	2.25	92.83 ± 1.52
GRB 180329B	819490	0.04	2.00	213.54 ± 49.42
GRB 180418A	826428	0.02	–	4.41 ± 2.49
GRB 180510B	831816	0.26	1.30	134.02 ± 52.92
GRB 180620A	843122	0.13	<1.2	22.95 ± 4.99
GRB 180624A	844192	0.05	2.85	466.65 ± 35.76
GRB 180626A	844615	0.04	–	30.10 ± 1.41
GRB 180705A	846299	0.06	–	106.78 ± 16.2
GRB 180706A	846395	0.02	–	42.44 ± 7.16
GRB 180809B	852553	0.16	–	233.24 ± 1.12
GRB 180812A	852903	0.04	–	16.53 ± 0.97
GRB 180904A	859282	0.04	–	4.63 ± 1.03
GRB 190427A	900730	0.06	–	0.19 ± 0.20
GRB 191011A	928924	0.02	1.72	7.35 ± 0.94
GRB 191016A	929744	0.09	3.29 ^b	126.68 ± 7.73
GRB 191031A	932435	–	–	19.10 ± 6.30
GRB 191031D	932608	0.08	–	0.29 ± 0.05
GRB 200122A	950330	0.03	–	190.60 ± 4.51
GRB 200125A	952164	0.08	–	350.34 ± 32.97
GRB 201021C	1001130	0.02	1.07	24.38 ± 6.76
GRB 210222B	1034325	0.10	2.20	12.11 ± 0.91
GRB 210504A	1046782	–	2.08	142.98 ± 9.33
GRB 210610A	1054627	0.03	3.54	13.62 ± 3.15
GRB 210610B	1054681	0.04	1.13	69.38 ± 2.53
GRB 210722A	1061223	0.03	1.14	50.20 ± 10.54
GRB 210822A	1069788	0.14	1.74	185.68 ± 46.63
GRB 220118A	1093742	0.03	–	10.61 ± 1.78

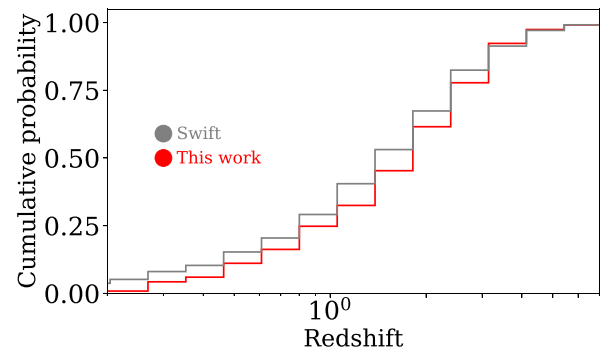
^aAnderson et al. (2018).^bSmith et al. (2021).

Figure 2. Comparison between the cumulative probability distribution of redshifts for the events in the sample used in this work and the redshifts of all GRBs in the *Swift*/BAT catalogue.

afterglow for GRBs (black line) with the corresponding 1σ deviation (grey regions).

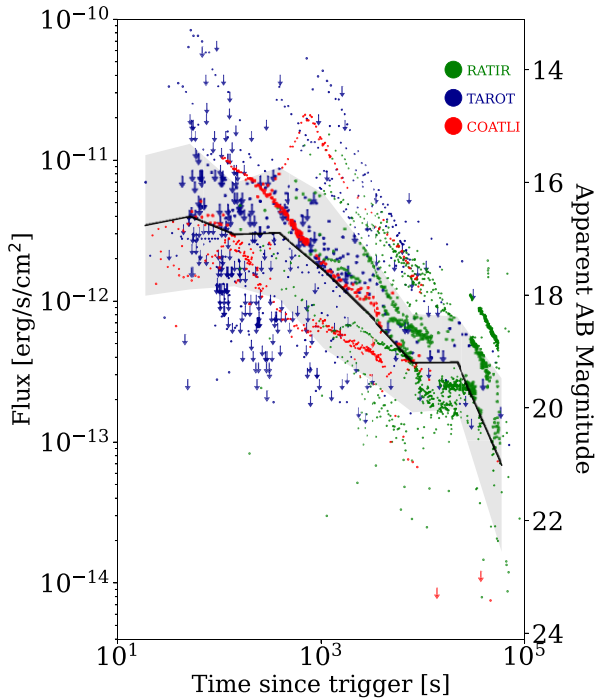


Figure 3. Optical detections and upper limits from TAROT (blue), RATIR (red), and COATLI (green) GRBs in the observed frame. Grey regions represent the 1σ dispersion from the average curve (black line).

4.1 Brightness function

Akerlof & Swan (2007) and Klotz et al. (2009) investigated the brightness function of GRBs at $T = 1000$ s. We adopt a similar approach here for the bright. We use only data between $T + 500$ s and $T + 2000$ s for interpolation (31 detections and 15 upper limits), compared to Akerlof & Swan (2007), who used the photometric information between $T + 100$ s and $T + 10000$ s, we refined our fit. For the cases where only a single data point (either detection or upper limit) was available, we estimate the magnitude at $T = 1000$ s using a power-law function $F \propto t^{-\alpha}$, with $\alpha = 1$ (Gehrels et al. 2004). In the case where multiple upper limits were available for the same event, we use the deepest upper limit for the calculation.

Fig. 4 presents the normalized cumulative probability histogram resulting from our analysis. We compare against a similar analysis performed with the data presented by Akerlof & Swan (2007; see their tables 1 and 2). However, to account for the difference with the limiting magnitudes of the facilities involved in our and their analyses, we only consider their data when the detections or upper limits are brighter than $r = 18.5$, which is the limiting magnitude of COATLI and TAROT with stacked images.

Following Klotz et al. (2009), we considered two scenarios for the upper limits: (i) an optimistic scenario, in which we assume that the non-detections lie just below the observed limiting magnitude (continuous lines in Fig. 4); (ii) a pessimistic scenario, in which we assume that the non-detections are even fainter than the faintest detected afterglow (dashed lines in Fig. 4). We also plot the average of these two scenarios (continuous thick lines in Fig. 4).

Under these assumptions, by comparing our result with that obtained by Akerlof & Swan (2007), we see a striking similarity in the brightness distribution. We estimate that about 20 per cent of the GRBs observed with telescopes such as COATLI or TAROT exhibit optical magnitude $r < 16$ and 75 per cent $r < 18$.

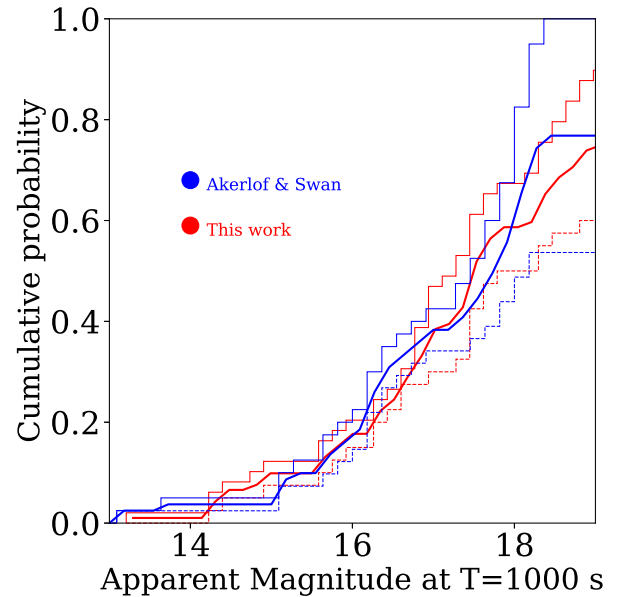


Figure 4. Cumulative optical brightness function obtained in this work at $T + 1000$ s for the detections and upper limits. We used the same criteria for pessimistic (dashed lines) and optimistic (solid lines) scenarios described by Klotz et al. (2009) for this work (Akerlof & Swan 2007) (blue). We also plot the mean distribution, for both samples in thicker solid lines.

4.2 Slope distribution

To gain further insight into the nature of the brightness function, we analyse the temporal index of the light curve determined for GRBs with more than one single point detected between $T + 500$ s and $T + 2000$ s. We fit a single power-law function to find the temporal index and the apparent magnitude at $T = 1000$ s. We illustrate this in the left-hand panel of Fig. 5. We found that the average α for detections is 0.80 ± 0.61 whereas the average apparent magnitude at 1000 s is 16.72 ± 1.36 . The uncertainties refer to the 1σ deviation from the average. The value of the temporal index is slightly larger than the one reported by Dainotti et al. (2022) and Srinivasaragavan et al. (2020) (at the end of the plateau phase). This is explained by the presence of flares, reverse shocks, and optical rebrightenings that can be found at earlier times. Fig. 5 shows no clear correlation, indicating that the afterglow decay rate is not a dominant parameter in the brightness of the early afterglow. We also determined in which phase of the light curve the GRBs are at time $T + 1000$ s, in order to distinguish the origin of the brightness, i.e. if the emission is produced by the typical decay of an afterglow or instead is due to an additional component (reverse shock, late central activity, etc.). For subsequent analysis and discussion, we distinguish events with previously identified reverse shock (stars) or late central activity components (squares). The figure shows that there is no clear correlation between the phase of the light curve and the observed magnitude.

The next step was to investigate the correlation between the apparent magnitude and the distance of the GRB. This is shown in the right-hand panel of Fig. 5. As might be expected, a slight trend is observed between the faintest and most distant GRBs. Nevertheless, the dispersion in the graph is too large to find a conclusive empirical relationship.

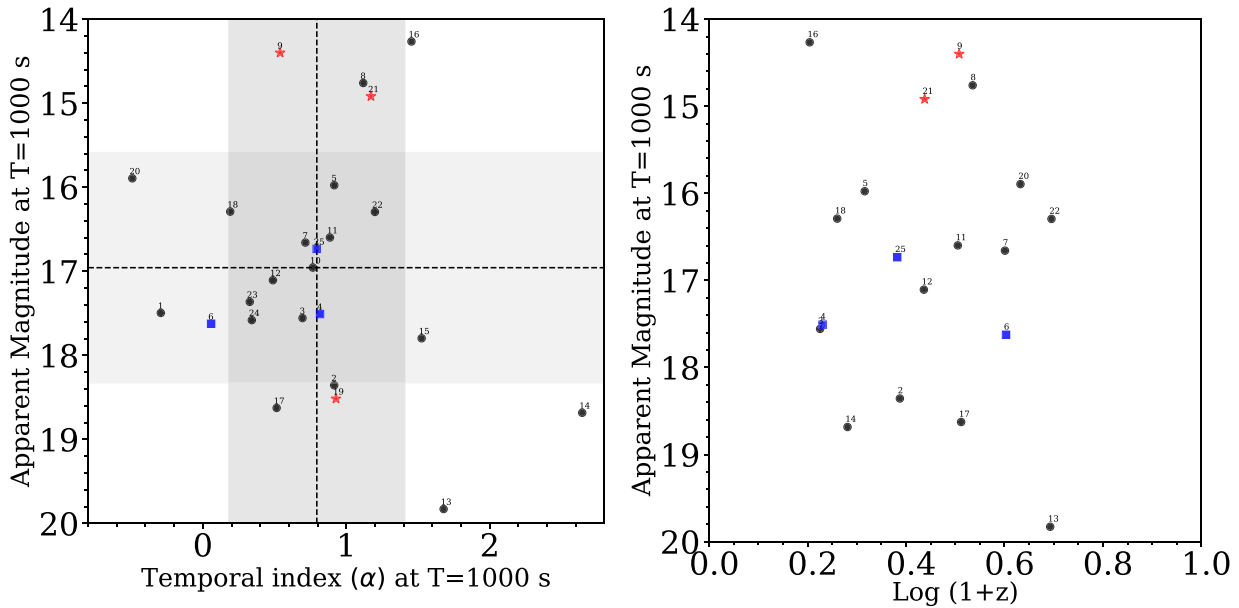


Figure 5. Left: Apparent optical magnitude versus temporal index α at $T + 1000$ s. We plot the mean values for the apparent magnitude and the temporal index at that time (dashed black lines) and the 1σ dispersion (grey area). Right: Apparent optical magnitude at $T + 1000$ s versus redshift. We distinguish the events with previously identified reverse shocks (red stars) or late central activity (blue squares). The numbers in the figure identify each GRB: 1. GRB 160127A, 2. GRB 180314A, 3. GRB 111209A, 4. GRB 060904B, 5. GRB 201021C, 6. GRB 070420, 7. GRB 141109A, 8. GRB 080413A, 9. GRB 110205A, 10. GRB 120913B, 11. GRB 210222B, 12. GRB 120119A, 13. GRB 120909A, 14. GRB 141225A, 15. GRB 130605A, 16. GRB 130215A, 17. GRB 180325A, 18. GRB 170519A, 19. GRB 180418A, 20. GRB 191016A, 21. GRB 210822A, 22. GRB 140419A, 23. GRB 150811A, 24. GRB 180812A, and 25. GRB 180205A.

4.3 Dark GRBs

Since the first detections of the afterglows in the 1990s, it has been evident that X-rays and optical light curves do not follow a canonical pattern or exhibit a standard relationship. The GRBs which are bright in X-rays and subluminal in optical, or even completely lacking the optical counterpart are called *dark* GRBs. Fynbo et al. (2001) and Lazzati, Covino & Ghisellini (2002) showed that a large fraction, about 60 per cent–70 per cent, of well-localized GRBs, has detections at optical wavelengths.

Lang et al. (2010) discussed three scenarios in which the optical emission is not present or is very weak compared to typical events: (i) absorption by the host galaxy or the surrounding gas (e.g. see Djorgovski et al. 2001; Fynbo et al. 2001), (ii) galactic absorption due to a high redshift, and (iii) intrinsic faintness of some GRBs.

While instruments such as COATLI (and even more TAROT) do not have the sensitivity to detect dark GRBs, they can constrain the X-ray-to-optical flux ratio at early times. The comparison of this ratio with the bright–dark limit defined by Jakobsson et al. (2004) may indicate if early measurements with instruments like COATLI or TAROT can quickly identify dark GRBs that require specific follow-up.

Jakobsson et al. (2004) proposed a definition of dark bursts based on the optical-to-X-ray spectral index $\beta_{\text{ox}} < 0.5$. This criterion has the advantage over others of leaving aside many of the factors, such as the collimation of the outflow and its density and depends on distance independent properties of the burst rather than distance-dependent ones (see e.g. Djorgovski et al. 2001) and only considers how the optical counterpart is compared to the fireball model.

We used this criterion for our sample. Using the *Swift*/XRT light-curve repository (Evans et al. 2007, 2009) hosted at the UK *Swift* Science Data Centre (UK SSDC), we selected only GRBs for which the X-ray data had a signal-to-noise ratio $S/N > 3$ at $T = 1000$ s. This

cuts the sample from 227 to 34. For these, our optical photometry gives 21 detections and 13 upper limits at $T + 1000$ s. These data are shown in Fig. 6. We also identified the better constraint events (with an evident temporal evolution) with filled markers and suspicious ones with unfilled markers, whose behaviour in the interpolation is ambiguous because of the presence of a plateau, reverse shock, flare, etc. We also plot different dashed lines showing the corresponding spectral index between the optical and X-rays. The *dark* region, in which $\beta_{\text{ox}} < 0.5$, is shown in grey in the figure.

Fig. 6 shows that all but one of the 34 GRBs lie above the bright–dark boundary, showing that the early identification of dark GRBs require instruments that are more sensitive than COATLI or TAROT. This will, however, become possible with COLIBRÍ, which reaches a limiting magnitude $R = 22$ in 1000 s (Basa et al. 2022).

In our sample, the distance (and therefore the hydrogen absorption in the optical bands due to high redshifts) is not a problem. Likewise, only one of the GRBs in the sample (the ultralong GRB 111205A) is indisputably dark under this criterion (whereas the upper limits for GRB 141031A and GRB 070508 make them likely candidates). This GRB shows a very different duration and energy-fluence than any other observed (Gendre et al. 2013; Greiner et al. 2015). Therefore, it supports the idea that it had a different origin from the populations that produce the common LGRBs and SGRBs (Gendre et al. 2013; Levan et al. 2014; Greiner et al. 2015).

5 PHYSICAL RESULTS

5.1 Redshift distribution

We calculate the redshift distribution for those GRBs in our sample that have redshift determinations following Porciani & Madau (2001). The number density of GRBs at redshift z about $z + dz$

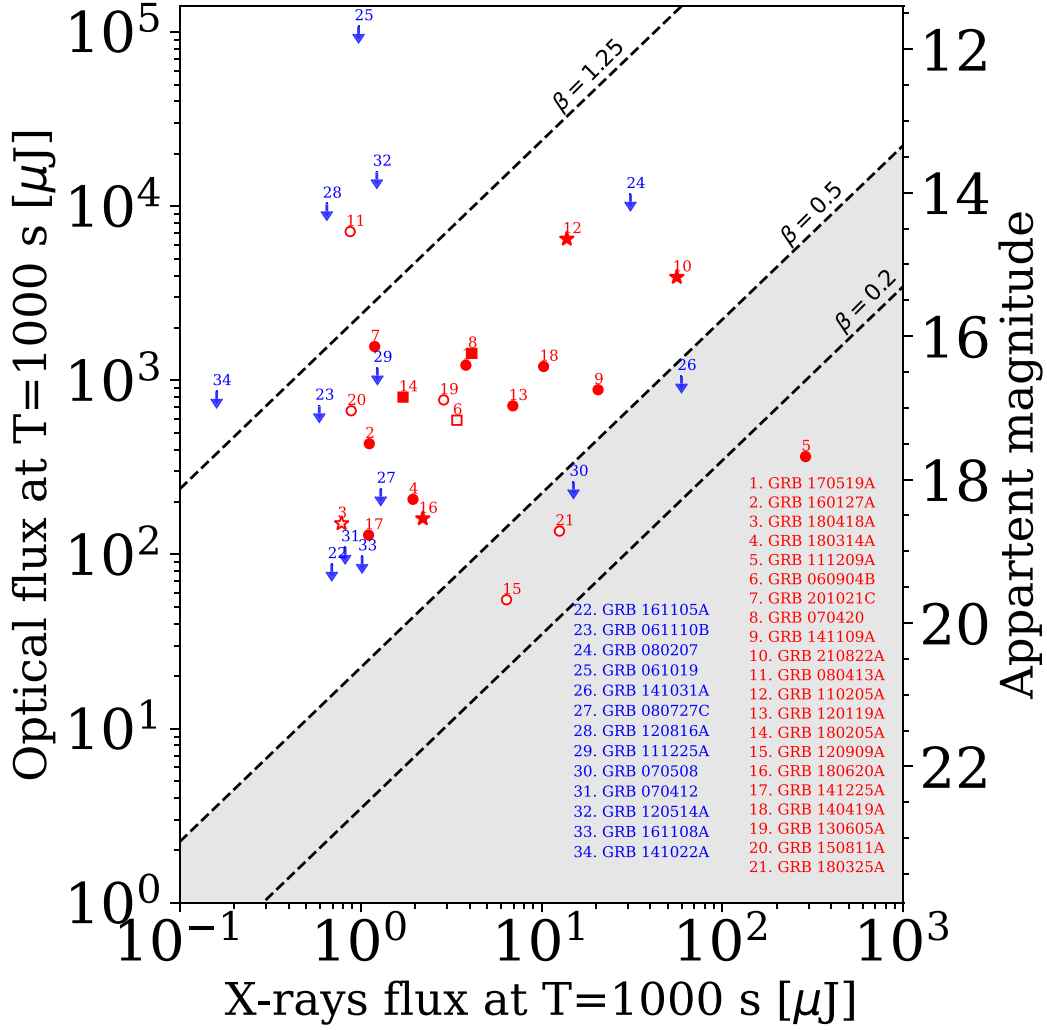


Figure 6. X-ray and optical fluxes at $T + 1000$ s. We show detections (red) and the upper limits (blue). The empty markers refer to events whose interpolation in the X-ray time range is uncertain. We illustrate the criteria proposed by Jakobsson et al. (2004) to identify dark GRBs (dashed black lines) and the dark GRBs region (grey area). The dashed lines, in particular, correspond to different values of the optical-to-X-ray spectral index β .

is given by:

$$n(z) = \frac{dN}{dz} = \frac{R_{\text{GRB}}(z) dV(z)}{1+z} \quad (1)$$

where $R_{\text{GRB}}(z)$ is the comoving GRB rate as a function of z , the factor $1/(1+z)$ accounts for the cosmological time dilation of the observed rate, and $\frac{dV(z)}{dz}$ is the comoving volume element. Assuming the star metallicity history from Kistler et al. (2008), Li (2008), and Virgili et al. (2011),

$$R_{\text{GRB}}(z) = \rho_0 R_{\text{SFR}}(z) (1+z)^\delta \Theta(\epsilon, z), \quad (2)$$

where ρ_0 is the local GRB rate (in units of $\text{Gpc}^{-3} \text{yr}^{-1}$), $(1+z)^\delta$ accounts for the possible effect of evolution of the GRB rate exceeding the star-forming rate (SFR), $\Theta(\epsilon, z)$ is the fractional mass density belonging to the metallicity below $\epsilon(Z_\odot)$ at a given z and (Z_\odot) refers to the solar metal abundance. We use the $R_{\text{SFR}}(z)$ reported by Porciani & Madau (2001) and Guetta & Piran (2007),

$$R_{\text{SFR}}(z) = \rho_0 \frac{23 \exp(3.4z)}{\exp(3.4z) + 22}. \quad (3)$$

$\Theta(\epsilon, z)$ is parametrized as Hopkins & Beacom (2006) and Langer & Norman (2006),

$$\Theta(\epsilon, z) = \frac{\hat{\Gamma}(\alpha + 2, \epsilon^\beta 10^{0.15\beta z})}{\Gamma(\alpha + 2)}, \quad (4)$$

where $\alpha = -1.16$ is the power-law index in the Schechter distribution function of galaxy stellar masses (Panter, Heavens & Jimenez 2004) and $\beta = 2$ is the slope in the linear bisector fit to the galaxy stellar mass–metallicity relation (Savaglio 2006; Li 2008), $\hat{\Gamma}$ and Γ are the incomplete and complete gamma function, respectively, $\epsilon = 0.4$, and $\delta = 0.4$ (Li 2008; Modjaz et al. 2008).

We fit equation (2) using TAROT, RATIR, and COATLI data and the values/functions described previously. We estimate a GRB rate of $\rho_0 = 0.2 \text{ Gpc}^{-3} \text{yr}^{-1}$ (dashed red line in Fig. 7) with a $\chi^2 = 2.63$ for GRB with redshift $z < 1$. This is only about 40 per cent of the total number of GRBs expected to be detected per year $\rho_0 = 0.5\text{--}1.0$ (Zhang 2018).

Previous studies have estimated the redshift–luminosity distribution of observed long *Swift* GRBs to obtain their rate and luminosity

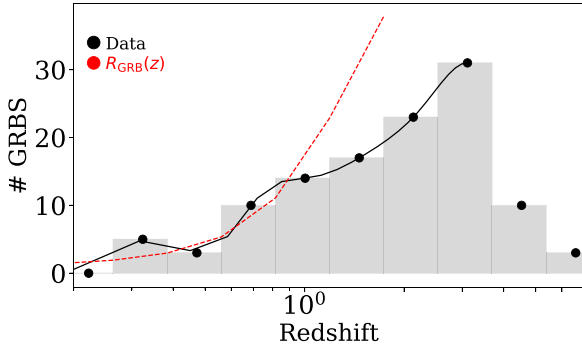


Figure 7. Histogram of the redshift distribution of our sample (grey bars) with the median of each bin (black points) and a smoothing function for better visualization (black line). We fit an $R_{\text{GRB}}(z)$ function (see in Section 5.1) obtaining a $\rho_0 = 0.2 \text{ Gpc}^{-3} \text{ yr}^{-1}$ (dashed red line) with a $\chi^2 = 2.63$ for GRBs with redshift $z < 1$. The information of redshifts was obtained from the *Swift* catalogue.

function. Wanderman & Piran (2010) described their sample with an increase for $0 < z < 3$ and a decrease for $z > 3$. The same qualitative behaviour was obtained by Petrosian, Kitanidis & Kocevski (2015) using a non-parametric determination for 200 *Swift* LGRBs with known redshifts and by Yu et al. (2015) using Monte Carlo simulations.

Our results are consistent with the fact that COATLI and TAROT can only observe a fraction of GRBs because of factors such as weather, maintenance, and observatory closures. Furthermore, we sometimes do not observe GRBs that have previously reported magnitudes or upper limits that are below our sensitivity.

Our estimation illustrates the difficulties present in these predictions based on biased samples with uncertain selection effects, as has been discussed by Dainotti et al. (2015) and Dainotti, Petrosian & Bowden (2021).

5.2 Canonical optical light curve

For each GRB in our sample with a redshift determination, we produced a rest-frame light curve, averaging the photometric information for each event over 20 equally spaced logarithmic intervals between the minimum and maximum values (see Fig. 3). We corrected for Galactic extinction. To account for cosmological effects in our sample, we use the cosmology calculator of Ned Wright⁷ (Wright 2006). We assume a Lambda cold dark matter model with $H_0 = 67.8 \text{ km s}^{-1} \text{ Mpc}^{-1}$ (Planck Collaboration 2014).

Fig. 8 shows the rest-frame light curves. It also shows the average light curve as a solid line and the 1σ dispersion about this average curve in grey regions.

Zhang et al. (2006) studied the X-ray light curves of GRBs and identified the different stages described in Section 1. According to Zhang et al. (2006), the first part of the X-ray curve is likely related to tail emission of the prompt phase. After this initial decay, there is a plateau phase decay between $T = 200 \text{ s}$ and $T = 5000 \text{ s}$. This segment suggests the presence of a continuing power source for the forward shock, which keeps being refreshed for some time. The most popular scenario is late central activity, that is, reactivation of the central engine. Nevertheless, it is not possible to reject other models such as a wide distribution of the shell Lorentz factors or the deceleration of a Poynting flux-dominated flow. That said, the presence of X-ray

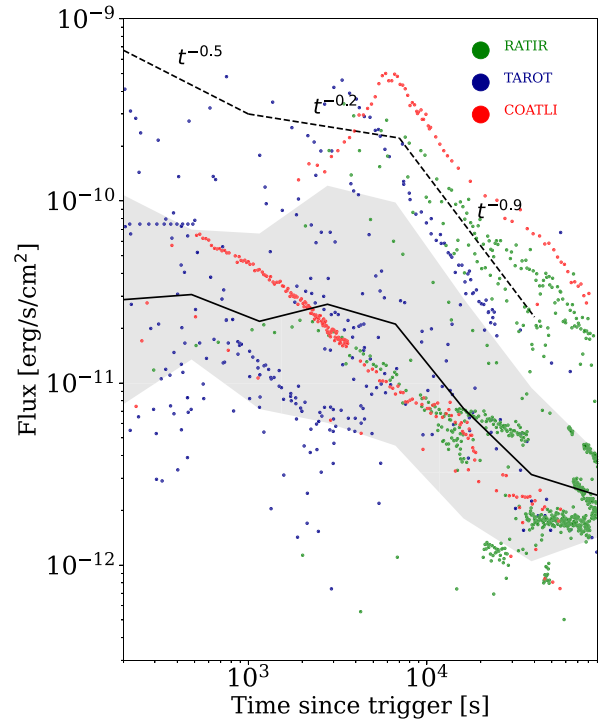


Figure 8. Optical detections from TAROT (blue), RATIR (green), and COATLI (red) GRBs in the rest frame and corrected for Galactic extinction. Grey regions represent the 1σ dispersion about the average curve (black line). We also plot the canonical behaviour and the corresponding temporal indices (dashed line) estimated in this work.

flares, around $T + 1000 \text{ s}$, suggests that the central engine is the source responsible for this continuing energy supply (Zhang et al. 2006). For $T > 10000$, we observe the theoretically predicted normal decay.

Similarly, the optical light curve obtained in this study can be interpreted as follows:

(i) $T < 1000 \text{ s}$: Beginning of the optical emission. Compared with X-rays, the early times of the optical emission suggest a different origin for this phase and are therefore not linked to the end of the prompt phase or internal shocks. We observe the signature of a shallow decay with an average temporal index of $\alpha = -0.5$ for $T < 1000$. This has been proposed to be the combination of reverse and forward shocks, such as in the cases of GRB 180418A (Becerra et al. 2019b), GRB 180620A (Becerra et al. 2019c), GRB 060904B, GRB 070420 (Klotz et al. 2008), and GRB 110205 (Gendre et al. 2013; Steele et al. 2017).

(ii) $1000 \text{ s} < T < 7000 \text{ s}$: We find a shallow temporal decay with $\alpha = -0.2$ in this interval. Nevertheless, the large dispersion illustrates the variety of features present. This might have its origin in the energy released by late central engine activity that produces a plateau phase or an optical flare (see e.g. Kumar & Zhang 2015; Zhang 2018; Becerra et al. 2019a; Pereyra et al. 2022).

(iii) $T > 7000 \text{ s}$: Optical counterpart of the normal decay observed in the X-ray canonical light curve, which is expected from the interaction between the head of the jet and the circumstellar medium. This has an average temporal index of $\alpha = -0.9$ (Kumar & Zhang 2015; Zhang 2018; Becerra et al. 2019c).

The phases identified here show the variety of processes and components that may be involved in early optical emission.

⁷<http://www.astro.ucla.edu/~wright/CC.python>

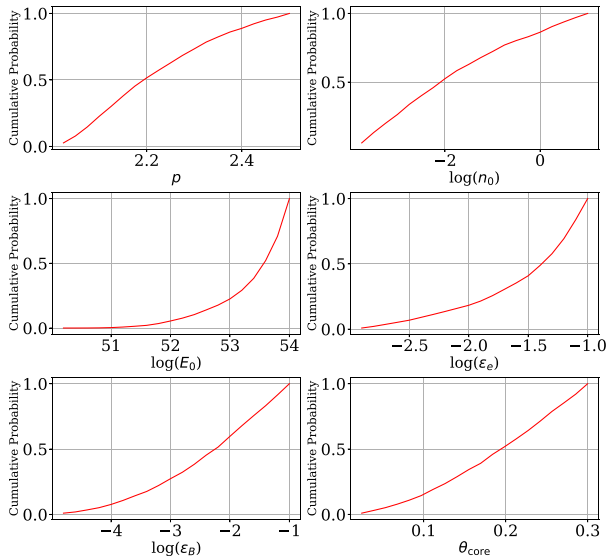


Figure 9. CDF of the parameters obtained by simultaneously fitting the average X-ray and optical light curves (shown in Fig. 8) using the AFTERGLOWPY (Ryan et al. 2020) library.

5.3 Parameters of the fireball model

The fireball model is typically used to describe the general behaviour of a GRB (Sari et al. 1998). This model relies on physical parameters of the jet such as energy E_0 , angle of aperture θ_{core} , electron index p , and thermal energy fractions in electrons ϵ_e and in the magnetic field ϵ_B (Sari et al. 1998). Additionally, the density n_0 of the medium surrounding the progenitor must also be considered (Sari et al. 1998; Granot et al. 2002).

These variables are often degenerate and there are numerous combinations that could produce a given light curve. To constrain the physics of the jet, we used the library AFTERGLOWPY (Ryan et al. 2020) to generate 100 000 different models with uniform random distributions of the parameters mentioned above. We assumed a structured jet for all the models (Urrutia et al. 2021; O’Connor et al. 2023) and compare with synthetic light curves that simultaneously deviated no more than 2σ from the average X-ray and optical light curves (see Fig. 8) in the range between $T + 200$ s and $T + 50000$ s. The cumulative distribution functions (CDFs) of these constrained parameters are presented in Fig. 9.

We determined the median values (corresponding to a cumulative probability of 0.5 in Fig. 9) for these parameters as follows: energy $E_0 \approx 10^{53.6}$ erg, opening angle $\theta_{\text{core}} \sim 0.2$ rad, density $n_0 \sim 10^{-2.1} \text{ cm}^{-3}$, $\epsilon_e \sim 10^{-1.37}$, magnetic field $\epsilon_B \sim 10^{-2.26}$, and index of electrons $p \sim 2.2$, which are typical values for GRBs (see e.g. Berger 2014; Santana, Barniol Duran & Kumar 2014; Fong et al. 2015; Levan et al. 2016), but ϵ_B is quite larger than previously measured (Santana et al. 2014).

6 DISCUSSION AND SUMMARY

We presented optical photometry of the prompt emission and afterglow of GRBs that were observed by TAROT, COATLI, and RATIR up to 2022. We obtained an average light curve in both the observer frame and the rest frame. We divided the results into two main categories: phenomenological and physical.

For the first part, a brightness distribution of our sample is calculated and compared to the values reported by Akerlof & Swan

(2007) and Klotz et al. (2009) at $T + 1000$ s. Nevertheless, the number of GRBs with reverse shock components or rebrightenings caused by late central activity makes it necessary to understand the behaviour of light curves beyond a simple decay. Therefore, we analyse the behaviour of the temporal indices for each GRB at this time. We observe a typical temporal index of $\alpha = 0.80 \pm 0.61$ for most of GRBs, but there are some cases where at that time a steeper decay (GRB 141225A) or a rapid rise (GRB 160127A and GRB 191016A) has been observed.

To investigate the nature of dark GRBs, we used the criterion proposed by Jakobsson et al. (2004), comparing the X-rays (from the *Swift*/XRT data base) and optical fluxes at $T + 1000$ s to evaluate how many of the optical fluxes correspond to those predicted by the fireball model.

Physically, using an analysis of the redshift distribution of our sample, we found a local GRB rate of $\rho_0 = 0.2 \text{ Gpc}^{-3} \text{ yr}^{-1}$ for GRBs with redshift $z < 1$. Therefore, compared to the lowest theoretical predictions, these collaborations were only able to observe about 40 per cent of the nearest GRBs.

Additionally, using the AFTERGLOWPY library, we have determined a set of parameters (energy, opening angle, etc.) that deviate by a maximum of 2σ from the average canonical curve in X-rays and optical frequencies.

Although in this analysis we have worked with GRBs with cosmological and extinction corrections, this sample is limited by the instrumental characteristics of the instruments involved. For example, using photometry from other networks such as the Rapid Telescopes for Optical Response (Vestrand et al. 2002), the Mobile Astronomical System of Telescope Robots (Lipunov et al. 2010, 2022), the Katzman Automatic Imaging Telescope (Li et al. 2003), and the Burst Observer and Optical Transient Exploring System (Castro-Tirado et al. 1999), we might have better coverage in terms of follow-up. Furthermore, given the sensitivities of each of these instruments, the data bases could complement each other very well. In the future, we plan to expand this study using data available from these collaborations. Moreover, the community will also have the possibility to expand the understanding of earlier stages of GRBs with the arrival of the COLIBRÍ telescope⁸ (Fuentes-Fernández et al. 2020; Basa et al. 2022; Nouvel de la Flèche et al. 2022, 2023). This optical–infrared telescope will offer significantly improved sensitivity compared to COATLI or TAROT but a similarly fast response. This will enable the estimation of GRB’s redshift within minutes, making the upcoming years crucial for advancing our understanding of the GRB phenomenon.

ACKNOWLEDGEMENTS

We thank our anonymous referee for comments that helped us significantly improve the discussion. TAROT has been built with the support of the Institut National des Sciences de l’Univers, CNRS, France. TAROT is funded by the CNES and thanks to the help of the technical staff of the Observatoire de Haute Provence, OSU-Pytheas. We thank the staff of the Observatorio Astronómico Nacional on Sierra San Pedro Mártir. Some of the data used in this paper were acquired with the COATLI telescope and interim instrument at the Observatorio Astronómico Nacional on the Sierra de San Pedro Mártir. COATLI is funded by CONACyT (LN 232649, 260369, and 271117) and the Universidad Nacional Autónoma de México (CIC and DGAPA/PAPIIT IT102715, IG100414, IN109408,

⁸<https://colibri.lam.fr>

and IN105921) and is operated and maintained by the Observatorio Astronómico Nacional and the Instituto de Astronomía of the Universidad Nacional Autónoma de México. RATIR is a collaboration between the University of California, the Universidad Nacional Autónoma de México, NASA Goddard Space Flight Center, and Arizona State University, benefitting from the loan of an H2RG detector and hardware and software support from Teledyne Scientific and Imaging. RATIR, the automation of the Harold L. Johnson Telescope of the Observatorio Astronómico Nacional on Sierra San Pedro Mártir, and the operation of both are funded through NASA grants NNX09AH71G, NNX09AT02G, NNX10AI27G, and NNX12AE66G, CONACyT grants INFR-2009-01-122785 and CB-2008-101958, UNAM PAPIIT grants IG100414, IA102917, and IN105921, UC MEXUS-CONACyT grant CN 09-283, and the Instituto de Astronomía of the Universidad Nacional Autónoma de México. The authors acknowledge the vital contributions of Neil Gehrels and Leonid Georgiev to the early development of RATIR. RLB acknowledges support from the CONAHcyT postdoctoral fellowship. This work made use of data supplied by the UK SSDC at the University of Leicester.

DATA AVAILABILITY

The data underlying this article will be shared on reasonable request to the corresponding author.

REFERENCES

- Abbott B. P. et al., 2017, *ApJ*, 848, L13
 Ahn C. P. et al., 2012, *ApJS*, 203, 21
 Akerlof C. W., Swan H. F., 2007, *ApJ*, 671, 1868
 Anderson M. M. et al., 2018, *ApJ*, 864, 22
 Atteia J.-L. et al., 2017, *ApJ*, 837, 119
 Basa S. et al., 2022, in Marshall H. K., Spyromilio J., Usuda T., eds, Proc. SPIE Conf. Ser. Vol. 12182, Ground-Based and Airborne Telescopes IX. SPIE, Bellingham, p. 121821S
 Becerra R. L. et al., 2017, *ApJ*, 837, 116
 Becerra R. L. et al., 2019a, *ApJ*, 872, 118
 Becerra R. L. et al., 2019b, *ApJ*, 881, 12
 Becerra R. L. et al., 2019c, *ApJ*, 887, 254
 Becerra R. L. et al., 2021, *ApJ*, 908, 39
 Becerra R. L. et al., 2023, *MNRAS*, 522, 5204
 Berger E., 2014, *ARA&A*, 52, 43
 Bertin E., 2010, Astrophysics Source Code Library. record ascl:1010.068
 Bertin E., Arnouts S., 1996, *A&AS*, 117, 393
 Burrows D. N. et al., 2005, *Science*, 309, 1833
 Butler N. et al., 2012, in McLean I. S., Ramsay S. K., Takami H., eds, Proc. SPIE Conf. Ser. Vol. 8446, Ground-Based and Airborne Instrumentation for Astronomy IV. SPIE, Bellingham, p. 844610
 Castro-Tirado A. J. et al., 1999, *A&AS*, 138, 583
 Cuevas S. et al., 2016, in Evans C. J., Simard L., Takami H., eds, Proc. SPIE Conf. Ser. Vol. 9908, Ground-Based and Airborne Instrumentation for Astronomy VI. SPIE, Bellingham, p. 99085Q
 Dainotti M. G., Del Vecchio R., Shigehiro N., Capozziello S., 2015, *ApJ*, 800, 31
 Dainotti M. G., Levine D., Fraija N., Warren D., Sourav S., 2022, *ApJ*, 940, 169
 Dainotti M. G., Petrosian V., Bowden L., 2021, *ApJ*, 914, L40
 Djorgovski S. G., Frail D. A., Kulkarni S. R., Bloom J. S., Odewahn S. C., Diercks A., 2001, *ApJ*, 562, 654
 Eichler D., Levinson A., 2000, *ApJ*, 529, 146
 Evans P. A. et al., 2007, *A&A*, 469, 379
 Evans P. A. et al., 2009, *MNRAS*, 397, 1177
 Fong W., Berger E., Margutti R., Zauderer B. A., 2015, *ApJ*, 815, 102
 Fuentes-Fernández J. et al., 2020, *J. Astron. Instrum.*, 09, 2050001
 Fynbo J. U. et al., 2001, *A&A*, 369, 373
 Gehrels N. et al., 2004, *ApJ*, 611, 1005
 Gendre B. et al., 2013, *ApJ*, 766, 30
 Gordon K. D., Clayton G. C., Misselt K. A., Landolt A. U., Wolff M. J., 2003, *ApJ*, 594, 279
 Granot J., Panaitescu A., Kumar P., Woosley S. E., 2002, *ApJ*, 570, L61
 Greiner J. et al., 2011, *A&A*, 526, A30
 Greiner J. et al., 2015, *Nature*, 523, 189
 Guetta D., Piran T., 2007, *JCAP*, 2007, 003
 Hopkins A. M., Beacom J. F., 2006, *ApJ*, 651, 142
 Jakobsson P., Hjorth J., Fynbo J. P. U., Watson D., Pedersen K., Björnsson G., Gorosabel J., 2004, *ApJ*, 617, L21
 Kann D. A. et al., 2010, *ApJ*, 720, 1513
 Kistler M. D., Yüksel H., Beacom J. F., Stanek K. Z., 2008, *ApJ*, 673, L119
 Klotz A., Boër M., Atteia J. L., Gendre B., 2009, *AJ*, 137, 4100
 Klotz A., Boër M., Eysseric J., Damerdjy Y., Laas-Bourez M., Pollas C., Vachier F., 2008, *PASP*, 120, 1298
 Klotz A., Gendre B., Stratta G., Atteia J. L., Boër M., Malacrino F., Damerdjy Y., Behrend R., 2006, *A&A*, 451, L39
 Kobayashi S., Piran T., Sari R., 1997, *ApJ*, 490, 92
 Kouveliotou C., Meegan C. A., Fishman G. J., Bhat N. P., Briggs M. S., Koshat T. M., Paciesas W. S., Pendleton G. N., 1993, *ApJ*, 413, L101
 Kumar P., Zhang B., 2015, *Phys. Rep.*, 561, 1
 Lang D., Hogg D. W., Mierle K., Blanton M., Roweis S., 2010, *AJ*, 139, 1782
 Langer N., Norman C. A., 2006, *ApJ*, 638, L63
 Lazzati D., Covino S., Ghisellini G., 2002, *MNRAS*, 330, 583
 Lee W. H., Ramirez-Ruiz E., 2007, *New J. Phys.*, 9, 17
 Levan A. J. et al., 2014, *ApJ*, 781, 13
 Levan A., Crowther P., de Grijs R., Langer N., Xu D., Yoon S.-C., 2016, *Space Sci. Rev.*, 202, 33
 Li L. et al., 2012, *ApJ*, 758, 27
 Li L.-X., 2008, *MNRAS*, 388, 1487
 Li W., Filippenko A. V., Chornock R., Jha S., 2003, *PASP*, 115, 844
 Liang E., Zhang B., Virgili F., Dai Z. G., 2007, *ApJ*, 662, 1111
 Lien A. et al., 2016, *ApJ*, 829, 7
 Lipunov V. et al., 2010, *Adv. Astron.*, 2010, 349171
 Lipunov V. M. et al., 2022, *Universe*, 8, 271
 Littlejohns O. M. et al., 2015, *MNRAS*, 449, 2919
 MacFadyen A. I., Woosley S. E., 1999, *ApJ*, 524, 262
 Magnier E. A. et al., 2020, *ApJS*, 251, 6
 Metzger B. D., Giannios D., Thompson T. A., Bucciantini N., Quataert E., 2011, *MNRAS*, 413, 2031
 Modjaz M. et al., 2008, *AJ*, 135, 1136
 Monet D. G. et al., 2003, *AJ*, 125, 984
 Nousek J. A. et al., 2006, *ApJ*, 642, 389
 Nouvel de la Flèche A. et al., 2022, in Holland A. D., Beletic J., eds, Proc. SPIE Conf. Ser. Vol. 12191, X-Ray, Optical, and Infrared Detectors for Astronomy X. SPIE, Bellingham, p. 121910Q
 Nouvel de la Flèche A. et al., 2023, *Exp. Astron.*
 O'Connor B. et al., 2023, *Sci. Adv.*, 9
 Paczynski B., 1986, *ApJ*, 308, L43
 Paczynski B., 1991, *Acta Astron.*, 41, 257
 Panter B., Heavens A. F., Jimenez R., 2004, *MNRAS*, 355, 764
 Pereyra M. et al., 2022, *MNRAS*, 511, 6205
 Perley D. A. et al., 2014, *ApJ*, 781, 37
 Petrosian V., Kitanidis E., Kocevski D., 2015, *ApJ*, 806, 44
 Planck Collaboration I, 2014, *A&A*, 571, A1
 Porciani C., Madau P., 2001, *ApJ*, 548, 522
 Rees M. J., Meszaros P., 1994, *ApJ*, 430, L93
 Ryan G., van Eerten H., Piro L., Troja E., 2020, *ApJ*, 896, 166
 Santana R., Barniol Duran R., Kumar P., 2014, *ApJ*, 785, 29
 Sari R., Piran T., Narayan R., 1998, *ApJ*, 497, L17
 Savaglio S., 2006, *New J. Phys.*, 8, 195
 Schlegel D. J., Finkbeiner D. P., Davis M., 1998, *ApJ*, 500, 525
 Skrutskie M. F. et al., 2006, *AJ*, 131, 1163
 Smith K. L. et al., 2021, *ApJ*, 911, 43

- Srinivasaragavan G. P., Dainotti M. G., Fraija N., Hernandez X., Nagataki S., Lenart A., Bowden L., Wagner R., 2020, *ApJ*, 903, 18
- Steele I. A. et al., 2017, *ApJ*, 843, 143
- Thompson C., 1994, *MNRAS*, 270, 480
- Tody D., 1986, in Crawford D. L., ed., Proc. SPIE Conf. Ser. Vol. 627, Instrumentation in astronomy VI. SPIE, Bellingham, p. 733
- Urrutia G., De Colle F., Murguía-Berthier A., Ramírez-Ruiz E., 2021, *MNRAS*, 503, 4363
- Vestrand W. T. et al., 2002, in Kibrick R. I., ed., Proc. SPIE Conf. Ser. Vol. 4845, Advanced Global Communications Technologies for Astronomy II. SPIE, Bellingham, p. 126
- Virgili F. J., Zhang B., Nagamine K., Choi J.-H., 2011, *MNRAS*, 417, 3025
- Wanderman D., Piran T., 2010, *MNRAS*, 406, 1944
- Wang X.-G., Liang E.-W., Li L., Lu R.-J., Wei J.-Y., Zhang B., 2013, *ApJ*, 774, 132
- Watson A. M. et al., 2012, in Stepp L. M., Gilmozzi R., Hall H. J., eds, Proc. SPIE Conf. Ser. Vol. 8444, Ground-Based and Airborne Telescopes IV. SPIE, Bellingham, p. 84445L
- Watson A. M. et al., 2016, in Evans C. J., Simard L., Takami H., eds, Proc. SPIE Conf. Ser. Vol. 9908, Ground-Based and Airborne Instrumentation for Astronomy VI. SPIE, Bellingham, p. 99085O
- Woosley S. E., 1993, *ApJ*, 405, 273
- Wright E. L., 2006, *PASP*, 118, 1711
- Yu H., Wang F. Y., Dai Z. G., Cheng K. S., 2015, *ApJS*, 218, 13
- Zhang B., 2018, *The Physics of Gamma-Ray Bursts*. Cambridge Univ. Press, Cambridge
- Zhang B., Fan Y. Z., Dyks J., Kobayashi S., Mészáros P., Burrows D. N., Nousek J. A., Gehrels N., 2006, *ApJ*, 642, 354
- Zhang B., Yan H., 2011, *ApJ*, 726, 90

This paper has been typeset from a \TeX/L\AA\TeX file prepared by the author.